

Contents lists available at [ScienceDirect](#)

Journal of Rock Mechanics and Geotechnical Engineering

journal homepage: www.jrmge.cn

Self-sealing of fractures in indurated claystones measured by water and gas flow

Chun-Liang Zhang^{a,*}, Jean Talandier^b^a Gesellschaft für Anlagen- und Reaktorsicherheit (GRS), Braunschweig, 38122, Germany^b Agence nationale pour la gestion des déchets radioactifs (ANDRA), Châtenay-Malabry cedex, 92298, France

ARTICLE INFO

Article history:

Received 30 September 2021
 Received in revised form
 26 November 2021
 Accepted 20 January 2022
 Available online xxx

Keywords:

Claystone
 Self-sealing of fracture
 Fracture closure
 Water permeability
 Gas breakthrough pressure
 Resealing of gas pathway

ABSTRACT

Self-sealing of fractures in the indurated Callovo-Oxfordian (COX) and Opalinus (OPA) claystones, which are considered as host rocks for disposal of radioactive waste, was investigated on artificially fractured samples. The samples were extracted from four lithological facies relatively rich in clay mineral, carbonate and quartz, respectively. The self-sealing of fractures was measured by fracture closure, water permeability variation, gas penetration, and recovery of gas-induced pathways. Most of the fractured samples exhibited a dramatic reduction in water permeability to low levels that is close to that of intact rock due to their mineralogical composition, fracture intensity, confining stress, and load duration. The self-sealing capacity of the clay-rich samples is higher than that of the carbonate-rich and sandy ones. Significant effects of sample size and fracture intensity were identified. The sealed fractures become gas-tight for certain injection pressures. However, the measured gas breakthrough pressures are still lower than the confining stresses. The gas-induced pathways can recover when contacting water. These important findings imply that fractures in such indurated claystones can effectively recover to hinder water transport but allow gas release without compromising the rock integrity.

© 2022 Institute of Rock and Soil Mechanics, Chinese Academy of Sciences. Production and hosting by Elsevier B.V. This is an open access article under the CC BY-NC-ND license (<http://creativecommons.org/licenses/by-nc-nd/4.0/>).

1. Introduction

The indurated Callovo-Oxfordian (COX) and Opalinus (OPA) clay formations have been proposed as host rocks for deep geological disposal of radioactive waste in France (Andra, 2005) and in Switzerland (Nagra, 2002), respectively. The clay formations have favourable properties for sitting of repositories such as extremely low permeability, diffusion-dominated transport and high sorption capacity for radionuclides, and certain self-sealing capacity. However, excavation of an underground repository will unavoidably generate an excavation damaged zone (EDZ) around the opening and can rise the permeability up to several orders of magnitude, as observed in the Underground Research Laboratories (URLs) at Bure (Armand et al., 2014; de La Vaissiere et al., 2015) and Mont-Terri (Bossart et al., 2004, 2017; Hale et al., 2021). Thanks to the self-sealing capacity of claystones, a gradual hydraulic recovery of the EDZ can be expected during the post-closure phase to limit water

flow and radionuclide transport to the biosphere. Another concern is gas generation and migration. Over thousands of years, gases are produced mainly from anoxic corrosion of metallic materials remained in the repository (Rodwell et al., 1999). With accumulation of gases, gas pressure rises and may exceed certain thresholds to damage the integrity of the geological and engineered barrier system. Two important questions on the gas issue need to be addressed: (1) whether the EDZ after sealing can still allow gas release without posting overpressure to damage the host rock and engineered barriers; and (2) whether the gas-induced pathways can reseal to hinder transports of water and radionuclides.

In the last two decades, water and gas transports in fractured COX and OPA claystones have been extensively investigated in laboratory experiments (e.g. Bock et al., 2010; Zhang, 2011, 2013, 2015; Auvray et al., 2015; Giot et al., 2018; Donna et al., 2019) and also field experiments in URLs at Bure (de La Vaissiere et al., 2015) and Mont-Terri (Marschall et al., 2017). Most of the studies focused on self-sealing of fractures in the clay-rich facies of COX and OPA formations. Significant self-sealing capacities of the clay-rich claystones were evidenced by fracture closure and permeability reduction under combined effects of mechanical compression and water-induced clay swelling. Micro- and macro-cracks in the clay-

* Corresponding author.

E-mail address: chun-liang.zhang@grs.de (C.-L. Zhang).

Peer review under responsibility of Institute of Rock and Soil Mechanics, Chinese Academy of Sciences.

<https://doi.org/10.1016/j.jrmge.2022.01.014>

1674-7755 © 2022 Institute of Rock and Soil Mechanics, Chinese Academy of Sciences. Production and hosting by Elsevier B.V. This is an open access article under the CC BY-NC-ND license (<http://creativecommons.org/licenses/by-nc-nd/4.0/>).

rich claystones tend to seal to very low water permeabilities that are close to that of the intact rock, even at low confining stresses of 2–4 MPa within months to years. For gas entry and penetration through water-saturated and sealed fractures, even if pressures required to overcome the capillary thresholds of the sealed pathways are high, they are still lower than the confining stresses and threshold pressures in the intact rocks. This implies that gases generated in a repository can release preferably through the EDZ without compromising the integrity and barrier functions of the host rock and engineered barrier system.

As well known, the sedimentary clay formations consist of layered lithological facies with different mineralogical compositions, petrophysical and hydro-mechanical properties (Horseman et al., 1996; Mazurek et al., 2008; Bock et al., 2010). The COX formation consists of three major geological units: clay-rich unit at the base, transition unit and silty-carbonated unit (Robinet et al., 2015; Conil et al., 2018), while the OPA formation can be divided into three facies: clay-rich shaly, sandy carbonate-rich, and sandy facies (Thury and Bossart, 1999; Bossart et al., 2017). Fig. 1 shows the variations of major mineralogical compositions across the thickness of the COX formation. For the safe isolation of radioactive waste in the clay host rocks, all lithological facies need to be precisely characterized and well understood.

Following the previous studies on the self-sealing of the clay-rich claystones (Zhang, 2011, 2013, 2015), more investigations recently focused on self-sealing performance of fractures in the COX carbonate-rich and OPA sandy claystones. Long-term consolidation, water and gas flow experiments were undertaken on artificially fractured samples with different sizes and fracture intensities. Large samples of multi-decimeteric length were used to cover the mineralogical variability of the clay rock, particularly the COX carbonate-rich unit. Two specific apparatuses were developed for parallel testing on several samples under identical hydro-mechanical conditions. The self-sealing of fractures was characterized by fracture closure, water permeability reduction, gas breakthrough pressure, and recovery of gas-induced pathways. Results are analysed in this paper concerning different influence

factors such as mineralogical composition, sample size, fracture intensity, water or gas injection pressure, and confining stress.

2. Material and methods

2.1. Samples

Core samples were extracted from the three units (i.e. clay-rich unit, transition unit, and silty-carbonated unit) of COX and sandy facies of OPA in the URLs at Bure, and Mont-Terri, respectively. They have different mineralogical compositions, petrophysical and hydro-mechanical properties. Table 1 summarises the main mineralogical components of the claystones: clay mineral, carbonate and quartz. Compared to the COX clay-rich unit and OPA shaly facies, the COX carbonate-rich unit and OPA sandy facies have less clay minerals but more carbonates and quartz. The mineralogical composition of each facies displays a spatial variability. Kaufhold et al. (2013) and Houben et al. (2014) demonstrated that the OPA sandy facies is more heterogeneous on millimetre- to centimetre-scale than the shaly facies. For instance, the samples taken from the OPA sandy facies for the present tests showed a

Table 1

Main mineralogical components of the sandy and shaly facies of OPA formation and the carbonate- and clay-rich facies of COX formation.

Component	Content (%)				
	OPA sandy facies	OPA shaly facies	COX carbonate-rich unit	COX transition unit	COX clay-rich unit
Clay mineral	20–40 ^a	55–75 ^a	15–40 ^b	30–55 ^b	40–55 ^b
Carbonate	15–40 ^a	5–30 ^a	20–80 ^b	20–40 ^b	20–35 ^b
Quartz	30–45 ^a	5–25 ^a	20–40 ^b	20–40 ^b	17–27 ^b

^a Estimated based on Thury and Bossart (1999), Mazurek et al. (2008), Bock et al. (2010), Kaufhold et al. (2013).

^b Estimated based on Andra (2005), Robinet et al. (2015), Conil et al. (2018), and Giot et al. (2018).

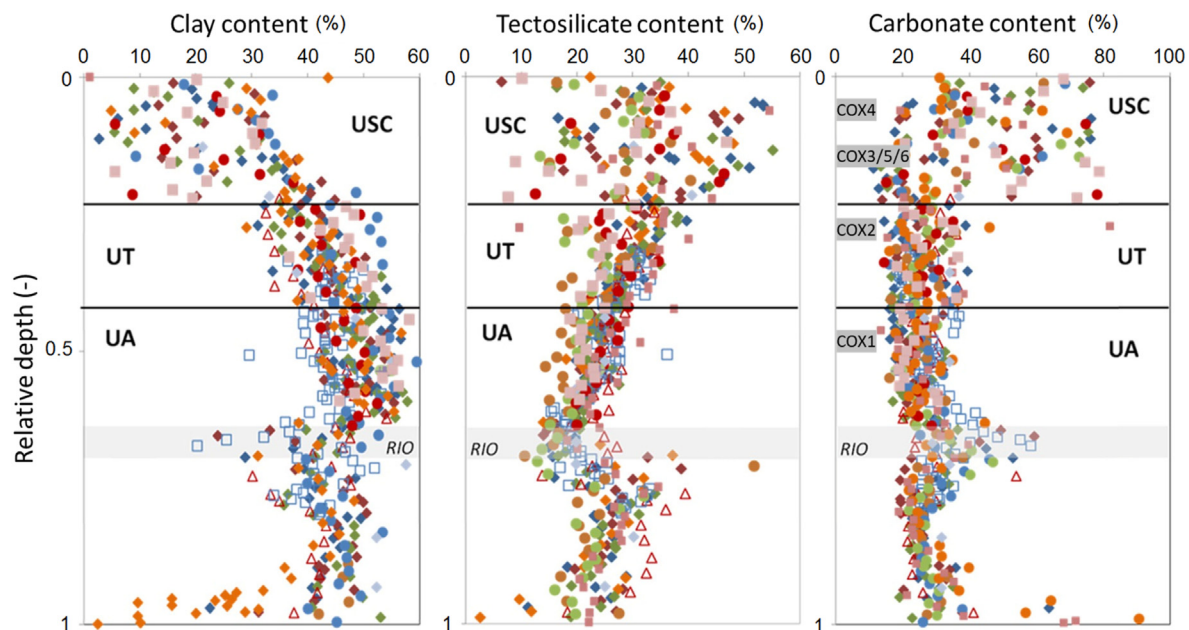


Fig. 1. Variation in mineralogical composition across the thickness of the COX formation. Data come from different boreholes and the relative depth is between the top of silty-carbonated unit and the bottom of clay-rich unit. UA represents the clay-rich unit at the base; UT denotes the transition unit; USC is the silty-carbonated unit; RIO is a small oolitic limestone layer.

large mineralogical variability within a short interval of 5 m with clay contents of 24%–39%, quartz of 34%–39%, carbonate of 15%–33%, and feldspar of 8%–9% (Table 2). Similarly, a mineralogical heterogeneity appears in the COX carbonate-rich unit on centimetre- to decimetre-scale as observed at a drift front at the –445 m level of the URL at Bure (Fig. 2). A sample from this area showed a large carbonate content of 50%, quartz of 25%, and a small clay content of 21% (Table 2).

The mineralogical heterogeneity can lead to local differences in deformability, swelling capacity, and thus self-sealing capacity of rock mass. Generally, the swelling capacity of a claystone is determined by the fraction of clay mineral. The previous swelling experiments (Zhang et al., 2010, 2019; Zhang, 2017) showed that the studied claystones possess certain swelling capacities with free volumetric expansion up to 10% at the COX clay-rich unit and OPA shaly facies and to 5% at the OPA sandy facies. The swelling with water uptake leads to degradation of the inner structure and reductions of stiffness and strength.

Ten samples were tested: four OPA sandy, two COX clay-rich, and four COX carbonate-rich. They were prepared to different sizes with diameter/length (D/L) of 50 mm/75–100 mm and 80 mm/280–300 mm. Their initial characteristics were determined before testing and are summarised in Table 3. The grain densities of the OPA and COX samples are nearly equal to 2.7 g/cm³. The dry density of the OPA sandy samples is slightly higher than that of the COX carbonate- and clay-rich ones. Due to sampling and long storage duration of 1–2 years, the samples were desaturated to some degree.

As observed in the field experiments in URLs at Bure and Mont-Terri (Armand et al., 2014; de La Vaissiere et al., 2015; Bossart et al., 2017; Hale et al., 2021), tensile fractures are mostly generated in the EDZ, which are responsible for increasing hydraulic conductivity. For laboratory testing, similar fractures were artificially generated in most of the samples by tensile cracking and/or direct splitting. Fig. 3 shows the fracture patterns produced in the samples. The samples were divided and tested in three groups:

- (1) Group 1: Three samples COX1, COX2 and OPA1 ($D/L = 50$ mm/75–100 mm) were inserted in rubber jackets and then cracked by Brazilian tensile loading along the length. A single major fracture was created in each sample (sub)parallel to the axis. The fracture apertures reached to around 1 mm. Some minor fissures appeared near the major one.
- (2) Group 2: Three (sub)parallel fractures were generated in two samples OPA2 and OPA3 ($D/L = 50$ mm/90 mm) at distance of around 15 mm. One fracture in OPA2 was however inclined to the outside surface and did not cross the other end face. The fracture apertures reached to approximately 1 mm. In OPA4, a regular fracture was produced by cutting an aperture of 30 mm wide and 2 mm opening through the length. The extremely high fracture densities in OPA2 and OPA3 and the single wide aperture in OPA4 do not really represent the EDZ in situ.



Fig. 2. Heterogeneous distribution of carbonates (light grey) in the COX carbonate-rich unit observed in a drift at the –445 m level of the URL at Bure.

- (3) Group 3: Four original large cores COX2 and COX4–6 ($D/L = 80$ mm/280–300 mm) were directly taken for examining scale effect on fracture sealing. Fractures were generated by pressing a steel wedge along the length, which caused several separate pieces with irregular shapes and surfaces. These pieces were then assembled in rubber jackets but could not be exactly matched together. The fracture patterns were complex with various directions, apertures, densities, and connections, as shown by the computed tomography (CT) images of the samples after testing. Note that white flecks on the CT images reflect the carbonates with high density, which distributed more in the samples COX4, COX5 and COX6 from the carbonate-rich unit than in COX2 from the transition unit.

Generally, most of the generated fractures with wide aperture of 1–2 mm and high density exhibited a similar scale of the in situ

Table 2

Main mineralogical components of some tested samples.

Lithological facies	Core No.	Borehole depth (m)	Content (%)				
			Clay	Quartz	Carbonates	Feldspar	Others
OPA sandy facies	BDM-B9-9	8.2	24	34	33	9	<1
	DBM-B9-18	10.2	36	39	15	9	<1
	DBM-B9-29	12.8	39	38	15	8	<1
COX carbonate-rich unit	EST52337	2.9	21	25	50	4	<1

Table 3
Initial characteristics of the claystone samples before testing.

Lithological facies	Drilled core	Depth/orientation	Sample No.	D/L (mm/mm)	Bulk density (g/cm ³)	Dry density (g/cm ³)	Porosity (%)	Water content (%)	Saturation degree (%)
OPA sandy facies	BLT-A10		OPA1	50/75	2.487	2.445	9.4	1.72	44
	BDM-B9-9		OPA2	50/90	2.515	2.478	8.2	1.49	45
	DBM-B9-18		OPA3	50/90	2.563	2.532	6.2	1.22	50
	DBM-B9-29		OPA4	50/90	2.559	2.527	6.4	1.27	50
COX clay-rich unit	EST49093	−482 m/V	COX1	50/100	2.383	2.262	16.2	5.35	75
COX transition unit	EST57262	−456 m/V	COX2	80/298	2.4	2.291	15.1	4.76	72
COX carbonate-rich unit	EST51223	−444 m/H	COX3	50/80	2.437	2.369	12.2	2.87	56
	EST52318	−437 m/V	COX4	80/283	2.584	2.553	5.4	1.21	56
	EST52335	−445 m/H	COX5	80/300	2.425	2.397	11.2	1.14	25
	EST52337	−445 m/H	COX6	80/280	2.434	2.405	10.9	1.21	27

Note: V and H represent vertical and horizontal directions, respectively.

macro-fractures near the rock walls but much larger micro-fractures than those in the deep areas of the EDZ as observed in the ULRs at Bure and Mont Terri (Armand et al., 2014; Hale et al., 2021). Furthermore, the artificially generated fractures in the samples are more intensively interconnected than the real fractures within the EDZ.

2.2. Test setups

Two setups were developed and used for water and gas flow testing on low permeable geomaterials under mechanical compression. Fig. 4 illustrate the layouts and apparatuses. The first setup (Fig. 4a) consists of three triaxial cells, which allow testing three samples of 50 mm in diameter and 70–120 mm in length in parallel under identical conditions. Axial and radial stresses were controlled by two separate syringe pumps. Another pump was applied to injecting water or gas into the samples via inlet lines and sintered porous discs at bottom. The inlet pressure was measured by a pressure transducer for each sample. The fluid outflow was recorded at the top of each sample using a scaled burette under atmospheric pressure. Deformation of each sample was recorded axially by a linear variable differential transducer installed at the top of the cell and laterally by a circumferential extensometer mounted at the middle of the length. The fractured samples in Groups 1 and 2 (Fig. 3a–f) were tested using this apparatus.

The second setup allows hydraulic testing on four samples with 80 mm in diameter and 200–300 mm in length in a pressure vessel (Fig. 4b). Each sample was inserted in a rubber jacket, covered by two sintered porous discs and two pistons, and tested in parallel under identical confining stress and fluid injection pressure. The confining stress was applied by a pressure-volume controller, while the water or gas injection was controlled by means of a syringe pump. The fluid outflow was recorded at the outlet of each sample using a burette under atmospheric pressure. This apparatus was used for testing the four large samples in Group 3 (Fig. 3g–j).

2.3. Test procedure

A common test procedure was designed and performed sequentially in the following steps:

- (1) Reconsolidation and water flow under effects of rock stress and porewater pressure

The reconsolidation and water permeability changes of the fractured samples were determined by injecting synthetic water under stepwise increased stresses. Synthetic COX and OPA

porewaters were produced according to their chemical compositions (Andra, 2005; Pearson et al., 2003) and were injected into the COX and OPA samples, respectively. The hydrostatic stress was stepwise increased up to 10 MPa for the samples of Group 1, 13 MPa for Group 2, and 4 MPa for Group 3, respectively. Stress range of 10–13 MPa selected for Groups 1 and 2 covers the lithostatic stresses surrounding the potential repository at a depth of about 500 m below the ground surface. The application of a low stress of 4 MPa to Group 3 is to examine impact of swelling pressure of a draft/shaft seal on the EDZ. Each step lasted for 1–4 months. The water injection pressure was adjusted in a range of 0.1–1 MPa that is much lower than the confining stresses to avoid hydraulic fracturing. During steady-state water flow, apparent water permeability was determined according to Darcy's law for incompressible fluids (Horseman et al., 1996):

$$K_w = \frac{Q_w \mu_w L}{A(P_w - P_o)} \quad (1)$$

where K_w is the water permeability (m²); Q_w is the water flow rate (m³/s); μ_w is the dynamic viscosity of the water (0.95×10^{-3} Pa s for the synthetic water); L is the sample length (m); A is the cross-section of the sample (m²); and P_w and P_o are the inlet and outlet water pressures (Pa), respectively.

- (2) Subsequent gas injection into the water-saturated and resealed fractures

Gas flow testing followed at the last load step by injecting helium gas into the water-saturated and sealed samples. Before gas injection, an attempt was made to remove the water remained in the inlet and outlet reservoirs. The gas injection pressure was stepwise increased at small increments of 0.1–0.2 MPa per day. As gas bubbles were first detected at the outlet side, the gas pressure in the inlet was defined as the breakthrough pressure. Beyond that, the gas injection continued to determine the apparent gas permeability according to Darcy's law for compressible fluids (Rodwell et al., 2003):

$$K_g = \frac{2Q_g \mu_g P_o L}{A(P_g^2 - P_o^2)} \quad (2)$$

where K_g is the gas permeability (m²); Q_g is the gas outflow rate (m³/s); μ_g is the dynamic viscosity of helium gas (1.96×10^{-5} Pa s); and P_g and P_o are the inlet and outlet gas pressure (Pa), respectively.

- (3) Resealing of gas-induced pathways after gas escape

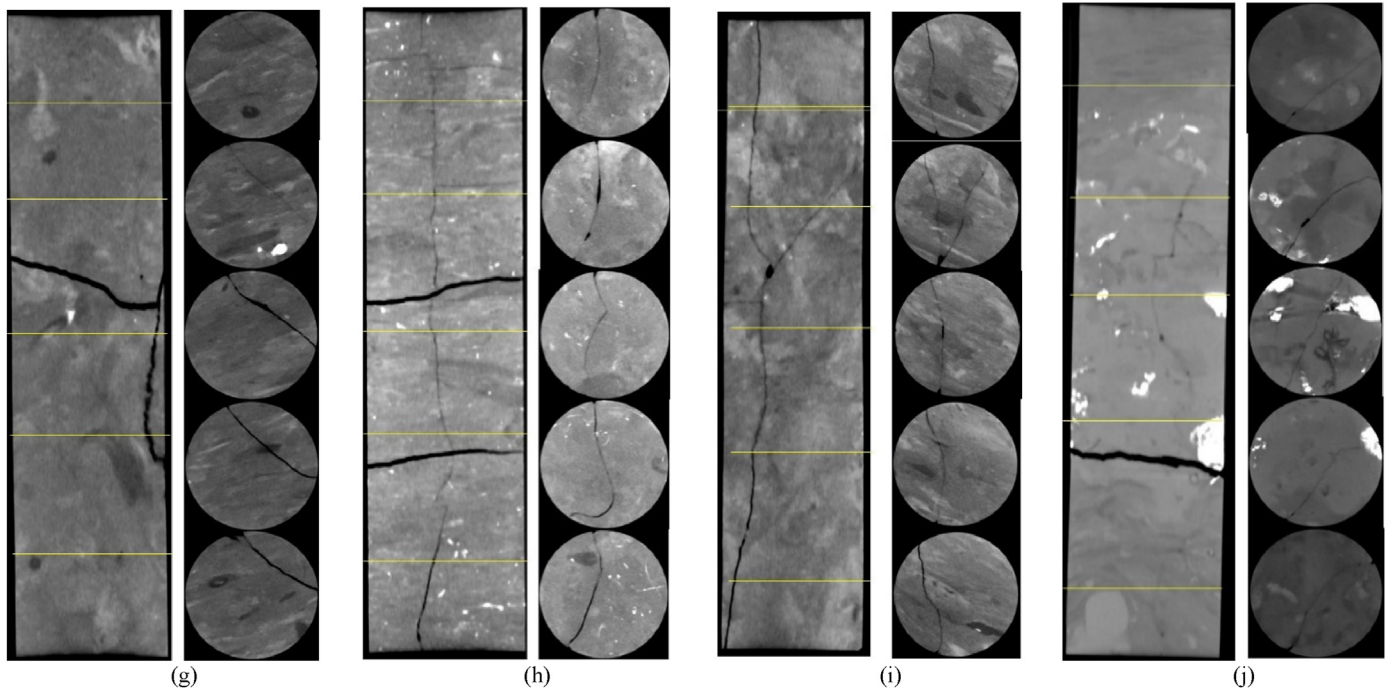
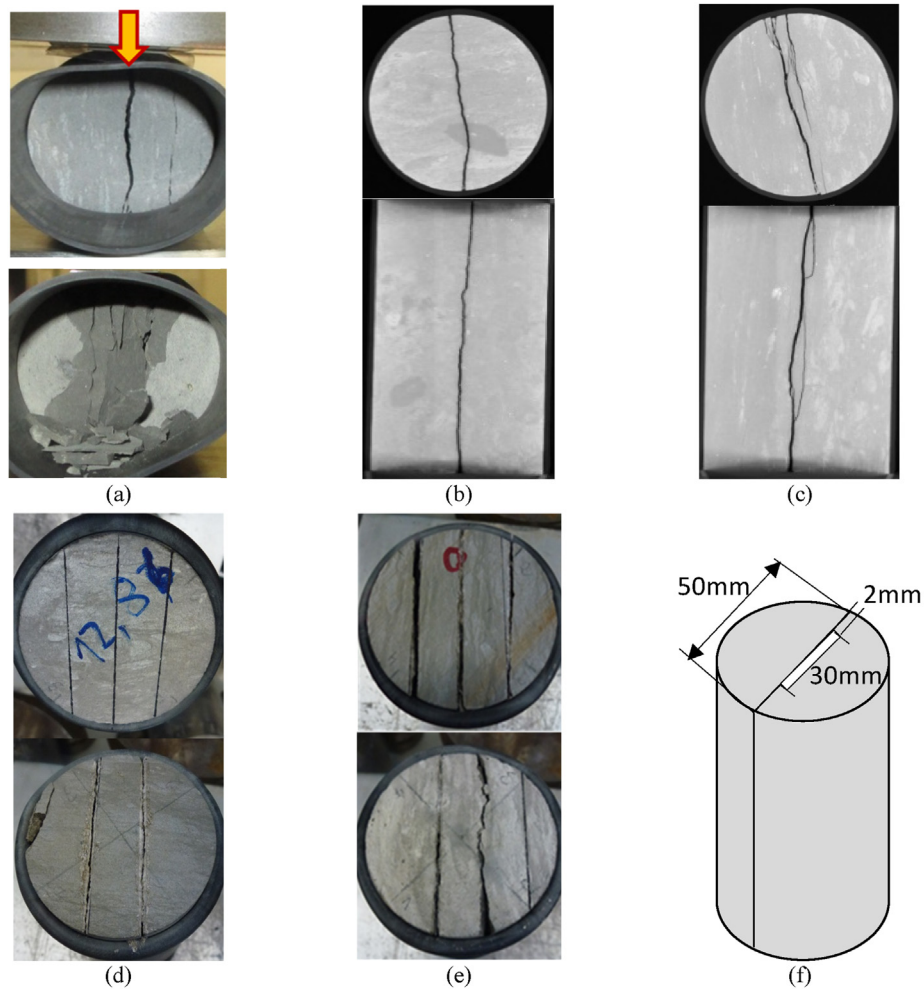
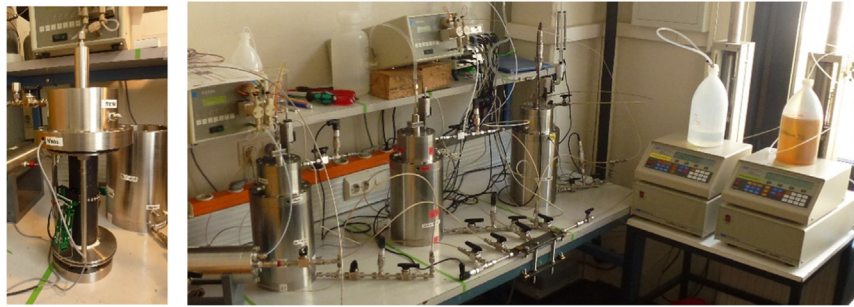
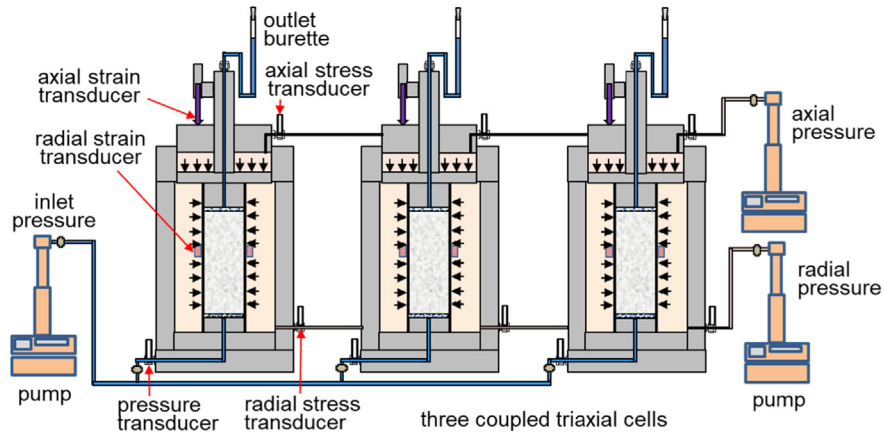
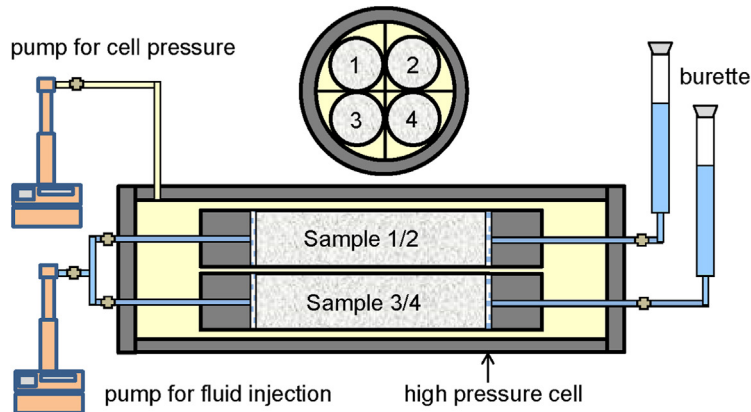


Fig. 3. Fracture patterns in the claystone samples illustrated with photos made before testing and CT images (Group 3) after testing: Group 1: (a) COX1, (b) COX3, and (c) OPA1; Group 2: (d) OPA2, (e) OPA3, and (f) OPA4; Group 3: (g) COX2 ($D/L = 80 \text{ mm}/298 \text{ mm}$), (h) COX4 ($D/L = 80 \text{ mm}/283 \text{ mm}$), (i) COX5 ($D/L = 80 \text{ mm}/300 \text{ mm}$), and (j) COX6 ($D/L = 80 \text{ mm}/280 \text{ mm}$).



(a)



(b)

Fig. 4. Two setups used for water and gas testing on fractured claystone samples: (a) Three parallel tests with triaxial cells under identical hydro-mechanical conditions, and (b) Four parallel tests in a pressure vessel under identical hydro-mechanical conditions.

Resealing of the gas-induced pathways was examined by reinjecting the synthetic water into the samples. The water permeability was measured to compare with that before the gas flow.

3. Results and discussion

3.1. Fracture closure and permeability change

3.1.1. Fracture closure

The fracture closure was measured by radial strain ϵ_r (sub) normal to the fracture planes along the length. Fig. 5 shows the typical process of fracture closure obtained on two fractured samples, OPA2 and OPA4, during water flow under multistep increased

stresses, together with axial strain ϵ_a parallel to the fracture planes and water permeability K_w . As already shown in Fig. 3d and f, OPA2 consisted of three axially (sub)parallel fractures with apertures of around 1 mm and at inter distance of around 15 mm; and OPA4 had a regular fracture geometry with a length of 30 mm and a wide aperture of 2 mm along the axis.

Firstly, a low hydrostatic stress of 0.5 MPa was applied without water injection to stabilize the fracture structure. Over a month, the fractures gradually closed with time to $\epsilon_r = 0.1\%$ at OPA2 and $\epsilon_r = 0.04\%$ at OPA4, respectively. The closure of the regular fracture in OPA4 is limited because of the strong resistance of the wide pillars on both end sides. In contrast, the closure of the irregular fractures in OPA2 is larger due to effect of high stress concentration on smaller contacting areas between the rough fracture walls.

As the synthetic water was injected into the fractures, a rapid swelling took place in all directions to strains of $\epsilon_a \approx \epsilon_r \approx 0.2\%$ at OPA2 and 0.3% at OPA4, respectively. The radial swelling observed externally indicates high local swelling pressures acting in contact areas between rough fracture surfaces, which exceed the external stress. Furthermore, the fracture walls expanded into the non-stressed interstices. This was demonstrated by submerging a fractured disc in the synthetic water without mechanical loading (Fig. 6a and b). The initial fracture opening of 2 mm was quickly filled by the swelling claystone as contacting water. The filling material became mud with low density and can be easily compacted under stress (Fig. 6c). The subsequent increase of the hydrostatic stress to 2 MPa, 3 MPa, 4 MPa, 6 MPa, and 10 MPa resulted in higher normal compaction compared to the parallel one, $\epsilon_r \approx 2\epsilon_a$. Under each constant stress, the strains evolved gradually with decreased rates until stabilisation. In correspondence with the compaction over 1.7 years, the water permeability decreased by 3–4 orders of magnitude to low values of $9 \times 10^{-20} \text{ m}^2$ at OPA2 and $1 \times 10^{-17} \text{ m}^2$ at OPA4, respectively.

In order to examine shearing effect on the fracture sealing, a deviatoric stress was applied by decreasing the radial stress to zero and increasing the axial stress to 13 MPa, $\sigma_a - \sigma_r = 13 \text{ MPa}$. This caused shear fractures inclined to the axis at angles of $30^\circ - 35^\circ$ (Fig. 6d and e). The relative shear movements of the separated matrixes disconnected the filled fractures partly. The combined effects of local normal compaction to close fracture aperture, shear deformation to disconnect fracture network, and clay swelling/slaking to seal fracture void are illustrated in Fig. 6f.

3.1.2. Water permeability

As a key parameter of fracture sealing, water permeability of each fractured sample was measured during water injection under increased stresses. The results are depicted in Fig. 7 for all samples.

Initially, the permeabilities of fractured samples were determined by gas injection at a pressure of 0.03 MPa and under the low stresses of 1 MPa for Groups 2 and 3 and 2 MPa for Group 1, respectively. High gas permeability were obtained to be $10^{-13} - 10^{-12} \text{ m}^2$ for all samples. As soon as the water was supplied, the fracture walls were wetted and expanded into the interstices and clogged the pathways (Fig. 6b). This decreased the permeability tremendously by several orders of magnitude to low values of $10^{-18} - 10^{-17} \text{ m}^2$ at the clay-rich facies of COX1 and COX2, $10^{-16} - 10^{-14} \text{ m}^2$ at the sandy ones of OPA1-4, and $10^{-15} - 10^{-13} \text{ m}^2$ at the carbonate-rich ones of COX3-6. The permeability reduction continued with time to lower values of $10^{-18} - 10^{-17} \text{ m}^2$ within 1–2 months for most samples. However, the carbonate-rich sample COX3 with a low clay content of 21% and two sandy ones OPA3 and OPA4 with high fracture intensities exhibited a limited permeability reduction to $10^{-15} - 10^{-14} \text{ m}^2$. During further consolidation at higher stresses, COX3 and OPA3 showed some fluctuations of the permeability. The dropping might reflect local collapse of fracture

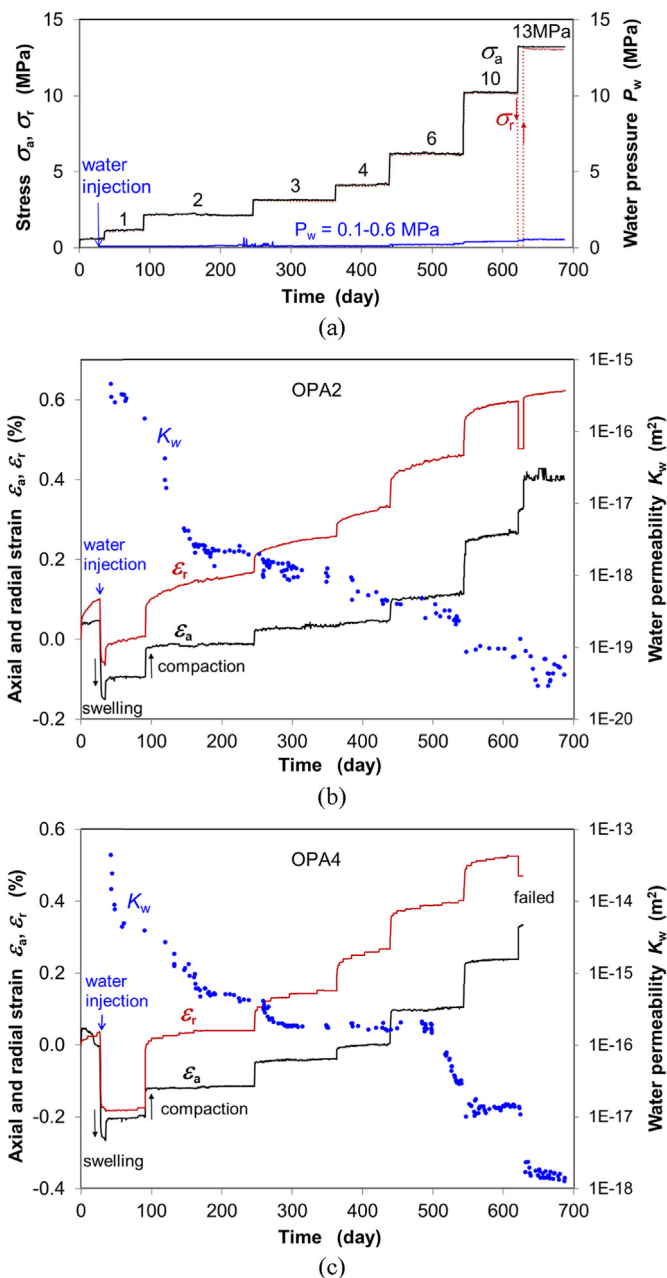


Fig. 5. Evolution of axial/radial strains and water permeability obtained on the sandy claystone samples OPA2 and OPA4 during water flow under stresses: (a) Applied confining stress and water injection pressure; (b) Resulted deformation and permeability change at OPA2; and (c) Resulted deformation and permeability change at OPA4.

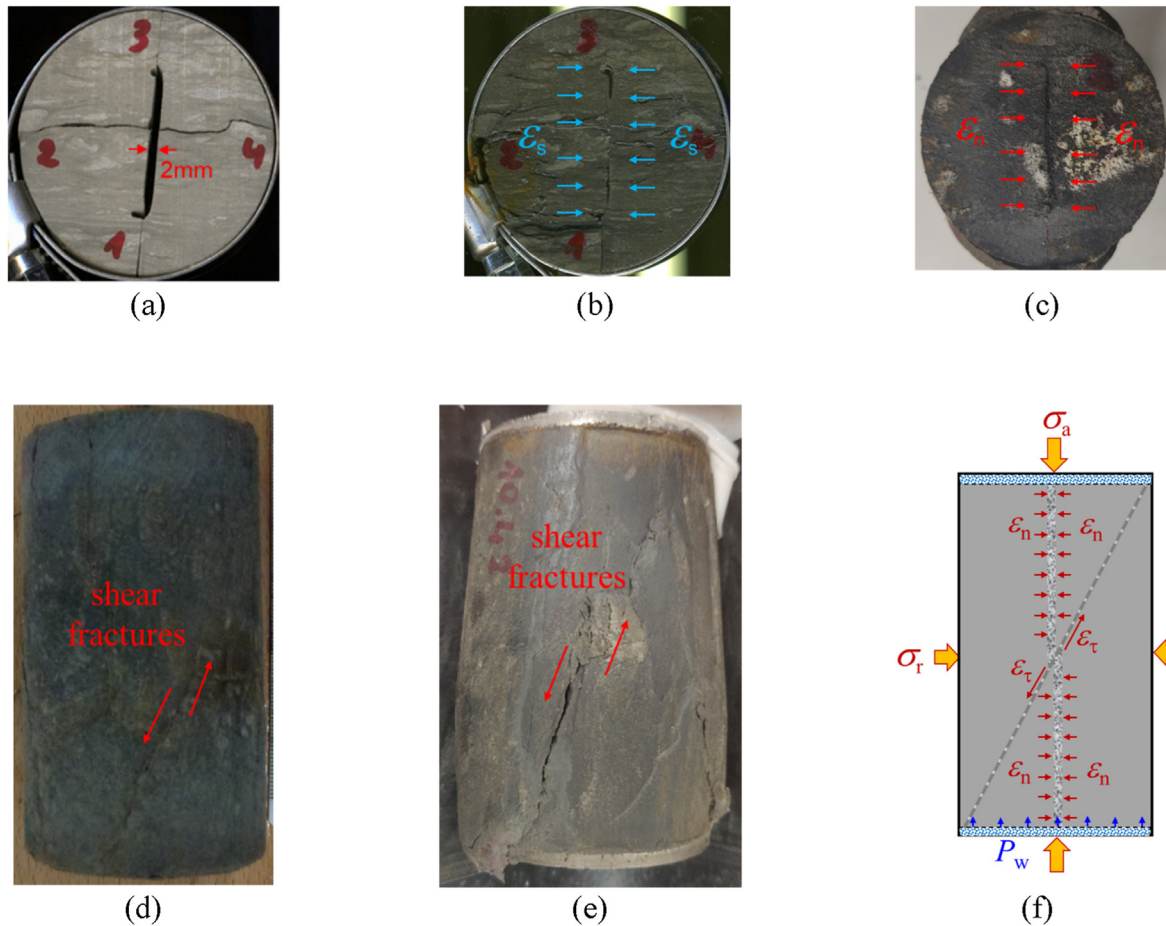


Fig. 6. Fracture sealing observed in the OPA sandy claystone samples under combined effects of water-induced swelling/slaking (ϵ_s), local normal and shear deformation (ϵ_n , ϵ_τ) under hydrostatic and shear stresses: (a) A fracture of 2 mm opening in a sandy claystone sample OPA4; (b) Filling of the fracture by water-induced swelling/slaking of fracture walls; (c) Normal compaction of the fracture under hydrostatic stress; (d) Shear fractures in (d) OPA2 and (e) OPA4 generated at a deviatoric stress of 13 MPa; and (f) Effects of normal and shear deformations and clay swelling on fracture sealing.

walls and clogging of the pathway, and on contrary, the rising might be caused by widening of some narrower pores due to possible erosion and movement of fine particles from the surfaces under relatively high injection pressures ($P_w = 0.1\text{--}1$ MPa). As mentioned earlier, the deviatoric stress applied to OPA2–4 in Group 2 sheared the matrix, disconnected the pathways locally, and hence decreased the permeability. Furthermore, by comparing the results from the different samples, more effects can be identified as follows:

(1) Effect of mineralogical composition

The samples in Group 1 with similar initial fractures (Fig. 3a–c) and under same load conditions (Fig. 7a) showed large differences in water permeability. K_w values of the clay-rich COX1 are one and four orders of magnitude lower than those of the sandy OPA1 and the carbonate-rich COX3, respectively. This is also true for the large samples with high fracture intensities in Group 3 (Fig. 7c), i.e. K_w values of the clay-rich COX2 being one order lower than those of the carbonate-rich COX4–6. As discussed above, the fracture sealing is determined mainly by the swelling capacity of the claystone, which is in turn determined by its clay content. The more clay content can take up more water, leading to more swelling and slaking of the fracture walls and clogging the interstices more effectively.

(2) Effect of fracture intensity

The OPA sandy samples in Groups 1 and 2 had been fractured to different geometries or intensities (Fig. 3a–f). The water permeabilities of samples OPA3 with three parallel fractures and OPA4 with a wide aperture of 2 mm (Fig. 7b) are 2–3 orders higher than those of the relatively less fractured ones, i.e. OPA1 with a single fracture (Fig. 7a) and OPA2 with three but one inclined to a dead end (Fig. 7b). This demonstrates the significance of fracture intensity (density, aperture, connectivity, etc.) for the fracture permeability, particularly for the initial value. With water flow, the initial sharp fracture patterns tend to disappear to mud with more homogeneously redistributed micropores (Fig. 6b). Further variation of the permeability with load is then more dominated by the consolidation of the mud and the stiffness of the surrounding claystone matrix.

(3) Scale effect

A scale effect can be recognised by comparing the water permeabilities of the large samples COX4–6 with lengths (L) of 280–300 mm (Fig. 7c) and the small one COX3 with $L = 80$ mm (Fig. 7a) from the same borehole in the carbonate-rich unit. The large samples, even though more intensively fractured (Fig. 3g–j), showed low K_w values of approximately 3×10^{-19} m² at a stress of

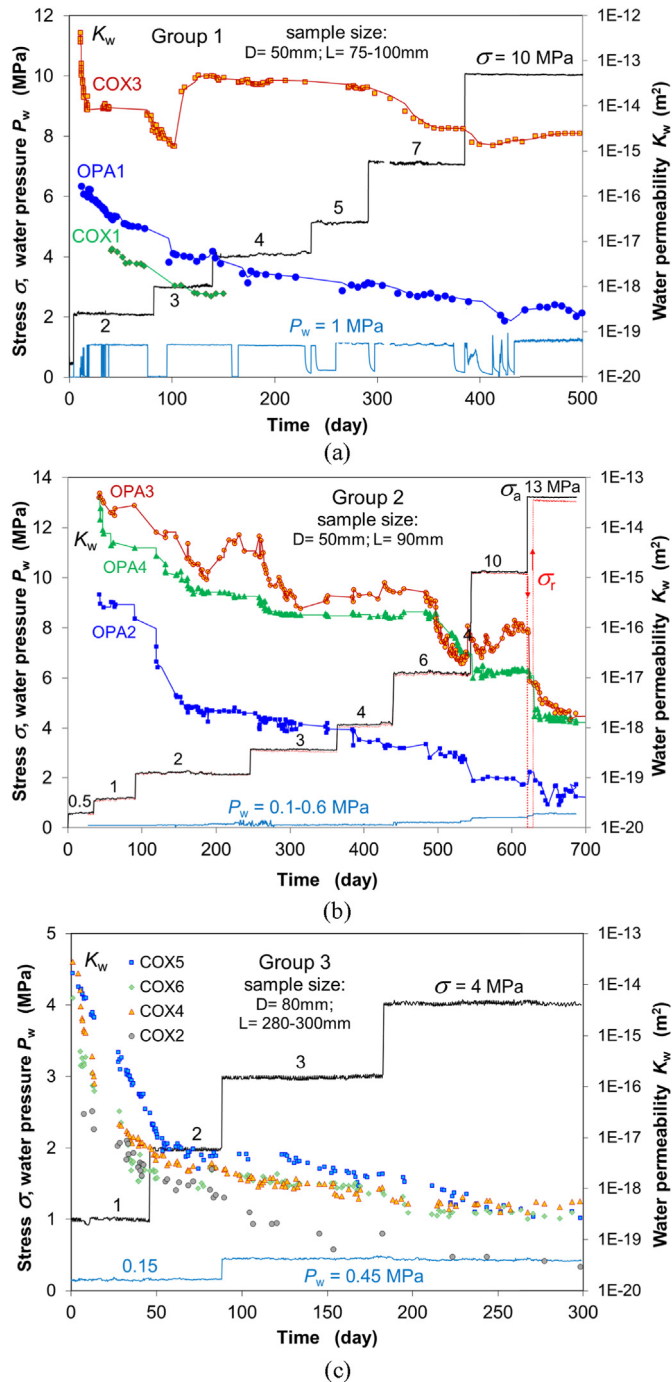


Fig. 7. Evolution of the water permeability measured on the fractured COX and OPA claystones during water injection under increased confining stresses: (a) Group 1, (b) Group 2, (c) Group 3.

4 MPa, being four orders of magnitude lower than that of the small sample even at high stress up to 10 MPa. As mentioned earlier, the distribution of carbonates is heterogeneous in form of bands on centimetre- to decimetre-scale (Fig. 2). If a fracture network is distributed through both carbonate-rich and clay-rich regions, the self-sealing performance of the entire network is determined mainly by the clay-rich part of the network. Therefore, it is important to take representative sample sizes for laboratory tests and sufficiently large areas for field experiments to provide reliable

data for the rock regions of interest, for instance, where seals will be constructed.

3.1.3. Stress dependence of fracture sealing

Two key parameters of the fracture sealing, i.e. fracture closure (or compaction) and water permeability, are strongly dependent on the applied stress. As a typical example, the radial and volumetric strains ($\varepsilon_r, \varepsilon_v$) and water permeabilities K_w obtained on samples OPA2 and OPA4 at the end of each load step (Fig. 5) are depicted in Fig. 8 as a function of effective hydrostatic stress ($\sigma_{eff} = \sigma - P_w/2$, where σ is the total stress). As mentioned earlier, the radial strain reflects the closure of fractures parallel to the sample axis. In case of the tests, there were also some micro-fractures randomly distributed and connected to the fracture network. Therefore, the volumetric strain is also needed for characterizing the sealing of the fracture network. The measured data in Fig. 8a and b shows that the fracture closure ($\varepsilon_r, \varepsilon_v$) increases nonlinearly and the associated water permeability decreases nonlinearly with increasing effective stress. In fact, the water permeability is directly related to the fracture closure, which can be approximately approached by

$$K_w = K_{wi} \exp(-\alpha \varepsilon_r) \quad (3)$$

where K_{wi} is the initial water permeability and α is a fitting parameter. The $K_w - \varepsilon_r$ data in Fig. 8c can be reasonably fitted by an empirical model with $\alpha = 8$ and $K_{wi} = 8 \times 10^{-18} m^2$ for OPA2 and $\alpha = 12$ and $K_{wi} = 2 \times 10^{-14} m^2$ for OPA4. The underestimation of the initial value for OPA2 is due to the lack of swelling/slaking effect at the beginning. A similar modelling result is also provided for the relation between water permeability and volumetric strain ($K_w - \varepsilon_v$) with $\alpha = 3$ for OPA2 and $\alpha = 4.5$ for OPA4 (Fig. 8d).

For purpose of comparison, the K_w data are summarised in Fig. 9 as a function of the effective stress for most samples including the previous results from the clay-rich samples COX7-10 (Zhang, 2013). The data from samples COX3, OPA3 and OPA4 are not involved because of the unrepresentative sample sizes and fracture intensities. The dependence of water permeability on effective stress can be approximated by

$$K_w = K_{wo} \exp(-\beta \sigma_{eff}) \quad (4)$$

where K_{wo} is the initial water permeability at zero effective hydrostatic stress ($\sigma_{eff} = 0$) and β is a parameter characterising the compressibility of the pathways.

As discussed above, the water-induced sealing of fractures and associated permeability reduction are strongly dependent on the clay content. As shown in Fig. 9, the clay-rich COX samples exhibited low initial permeabilities of $K_{wo} = 10^{-19} - 10^{-17} m^2$, lower than $K_{wo} = 10^{-17} - 10^{-16} m^2$ of the carbonate-rich COX and the sandy OPA ones. The permeability values are consistent with the in situ values of the EDZ observed in URLs at Bure and Mont-Terri (Bossart et al., 2004; de La Vaissiere et al., 2015). The slope of the $\log_{10} K_w - \sigma_{eff}$ curve varies with mineralogical composition and fracture intensity, which is reflected by the parameter β ranging from $0.15 MPa^{-1}$ to $0.8 MPa^{-1}$ for the samples. A high value of β implies a high significance of the mechanical impact on the fracture sealing.

Generally, the test results from the representative samples showed significant self-sealing of fractures in the clay-, carbonate- and sand-rich claystones. Most of the fractured samples reached low water permeabilities of $10^{-18} - 10^{-20} m^2$ even at relative low stresses of 2–4 MPa. These values are close to that of the intact claystone, determined to $4 \times 10^{-21} m^2$ on an intact clay-rich COX sample at a hydrostatic stress of 14 MPa and a pore pressure of 4.5 MPa, equivalent to the in situ conditions expected for the

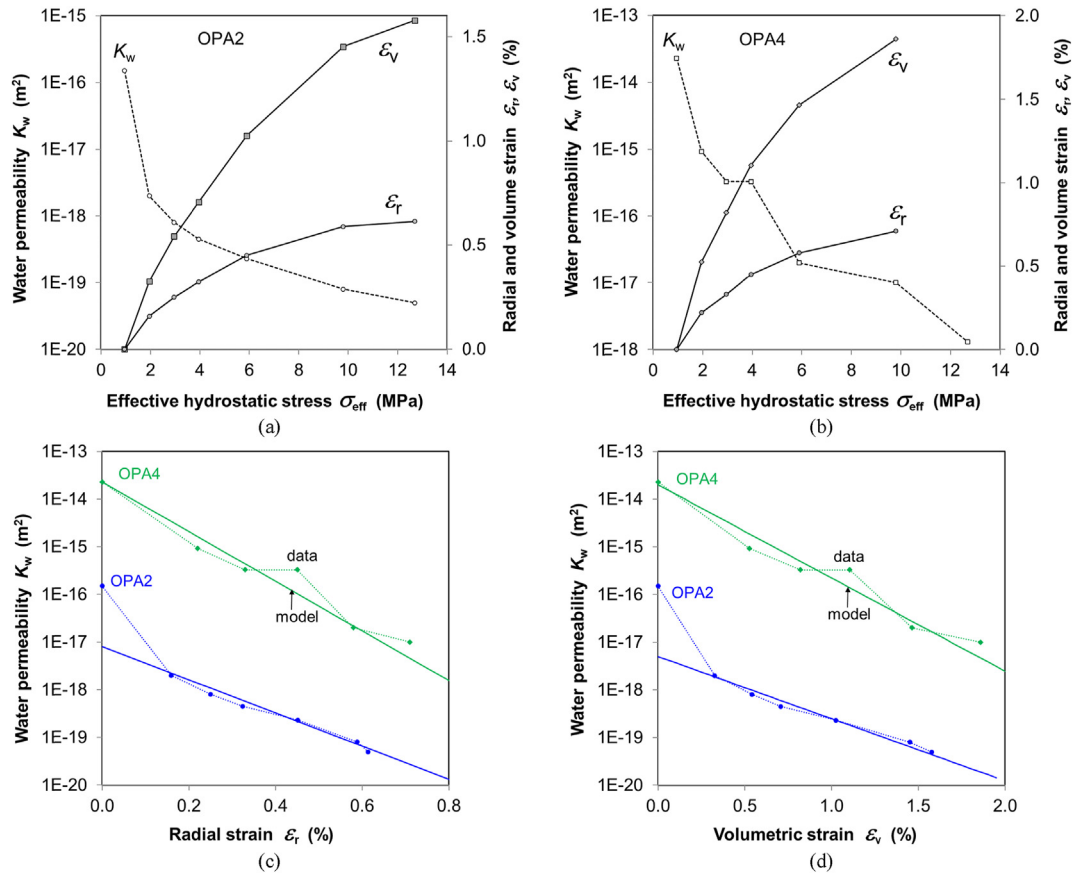


Fig. 8. Dependences of fracture closure (radial and volumetric compressions) and water permeability on effective hydrostatic stress: (a) OPA2 with a high initial fracture density and (b) OPA4 with a regular fracture aperture of 2 mm; water permeability in relation with (c) radial strain and (d) volumetric strain.

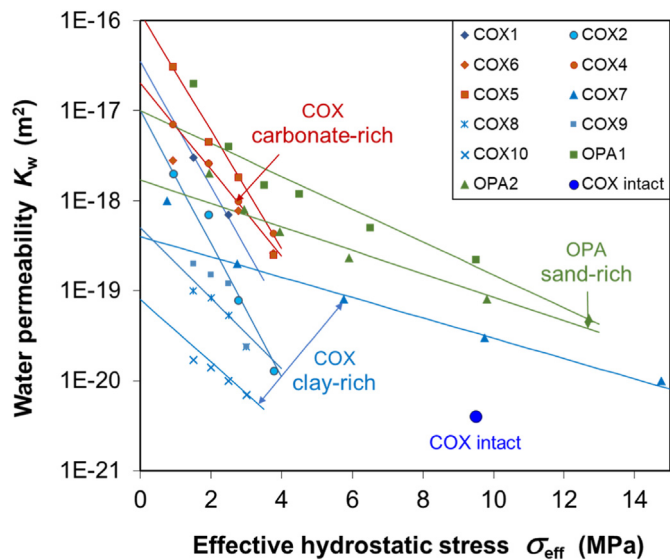


Fig. 9. Water permeabilities of the fractured claystone samples as a function of effective hydrostatic stress (blue colour for clay-rich COX, red for carbonate-rich COX, green for sandy OPA).

potential repository in the COX formation. By extrapolation of the test data to the in situ conditions, a complete recovery of the EDZ can be expected during a long-term consolidation phase of tens of thousands of years. This important conclusion needs to be

confirmed further with more representative samples in size and fracture intensity like the EDZ.

3.2. Gas penetration and impact

Gas testing followed the last consolidation stage at respective constant stress of 10 MPa, 13 MPa, and 4 MPa for the samples in Groups 1–3 respectively to investigate gas penetration through sealed fractures and recovery of gas-induced pathways. The results are illustrated in Figs. 10–12.

3.2.1. Gas penetration

Gas injection pressure P_g was stepwise increased with small increments of 0.1–0.3 MPa at a time interval of 1–3 d. As gas bubbles were detected at the outlet, the inlet pressure was defined as the gas breakthrough pressure P_b . In each group, the gas breakthrough took place sequentially starting from the weakly sealed sample at a low pressure to strongly sealed one under an increased pressure. For instance, the data in Fig. 10 show that the gas breakthrough occurred firstly at $P_b = 1.1$ MPa at the weakly sealed COX3 with a relatively high value of $K_w = 2 \times 10^{-15} \text{ m}^2$ and then followed at $P_b = 5.5$ MPa at the strongly sealed OPA1 with a low value of $K_w = 2 \times 10^{-19} \text{ m}^2$. Similar results were also obtained in other samples, as shown in Figs. 11 and 12. This suggests that the strongly sealed fractures possess high capillary thresholds, which can be overcome by higher pressures for gas penetration. After a network of gas pathways is generated under the breakthrough pressure, its gas permeability increases with increasing gas pressure. That may be caused by the generation of new fissures and

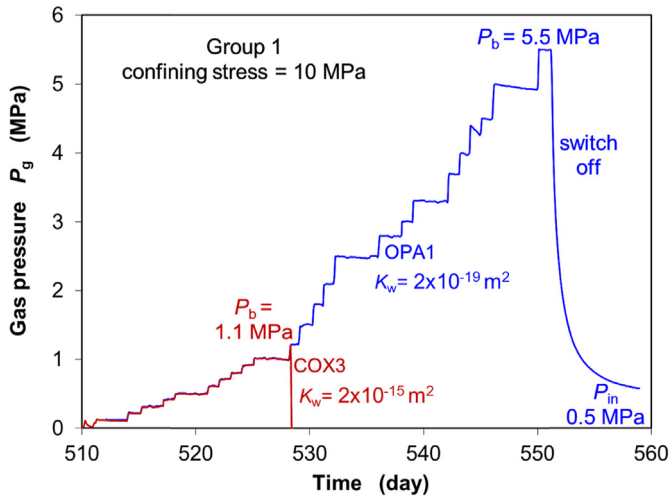


Fig. 10. Variation of gas breakthrough pressure of the samples in Group 1 at a hydrostatic stress of 10 MPa with time.

et al., 1995; Horseman et al., 1996; Rodwell et al., 1999), suggest that P_b is reciprocally dependent on the cube root of water permeability K_w :

$$P_b = B (K_w)^{-1/n} \tag{5}$$

where B is a parameter; and n is a constant, and $n = 3$. This relationship is also confirmed by previous experiments on the COX and OPA claystone samples with sealed fractures (Zhang, 2015). The gas breakthrough pressure is also related to the minimum principal stress σ_{min} :

$$P_b = B (K_{wo})^{-1/n} \exp(\lambda \sigma_{min}) \tag{6}$$

By fitting the present data in Table 4 and previous data in Zhang (2015), the parameters are obtained to be $B = 3.5 \times 10^{-7} \text{ MPa m}^{2/3}$, $n = 3$, $\lambda = 0.2 \text{ MPa}^{-1}$, and K_{wo} varying from $8 \times 10^{-20} \text{ m}^2$ to $1 \times 10^{-17} \text{ m}^2$ (Fig. 9). Fig. 13 shows a reasonable agreement between the model curves and test data. Obviously, the gas breakthrough pressure increases with decreasing initial water permeability and

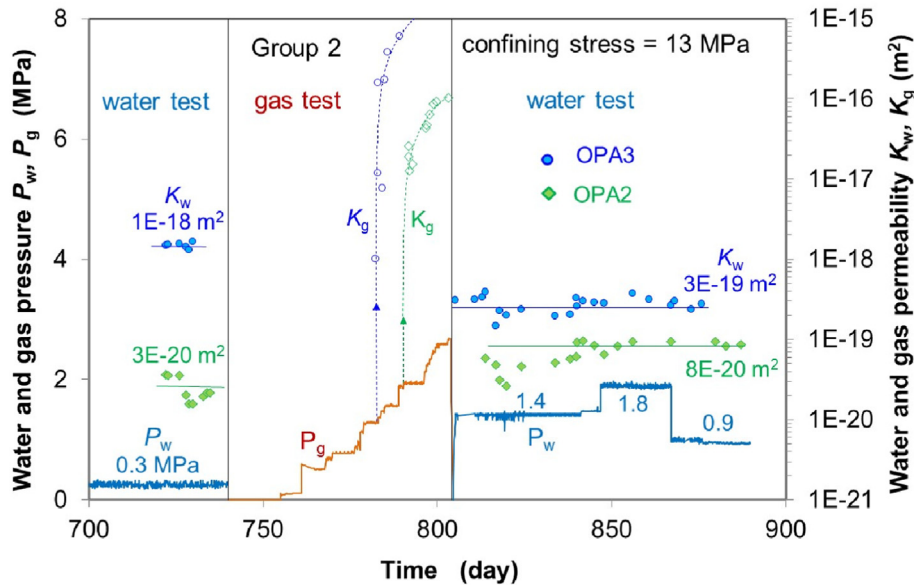


Fig. 11. Gas breakthrough pressures and permeability variations of the samples in Group 2 and resealing of gas pathways by water flow at a hydrostatic stress of 13 MPa.

dilatation of the pathways. As the gas injection was switched off after breakthrough (Fig. 10), the gas pressure fell and declined gradually with time to a lowest constant value. The minimum pressure is referred to as the shut-in pressure P_{in} , at which the pathway network is disconnected.

3.2.2. Gas breakthrough pressure

The measured gas breakthrough pressures are summarised in Table 4. As mentioned above, the gas breakthrough pressure depends on the sealing intensity of the fractures, which can be represented by the intrinsic or water permeability. Extensive theoretical studies and experimental measurements on rock samples in laboratory and in different rock masses, such as plastic clay, indurated shale, limestone, anhydrite, and bedded salt (Volckaert

increasing stress. This model can also capture the high gas breakthrough pressures of 10–12 MPa measured both on intact COX and OPA samples (Romero and Gómez, 2013; Harrington et al., 2017) and in the rock mass (de La Vaissiere et al., 2015). However, all the gas breakthrough pressures observed do not reach the gas fracturing threshold P_{fr} of the rocks:

$$P_b < P_{fr} = \sigma_{min} + \sigma_T \tag{7}$$

where σ_T is the tensile strength of 1–2 MPa for the intact claystones (Bock et al., 2010). Because the gas breakthrough pressures of the sealed claystones are always lower than the intact ones, the EDZ, even when highly sealed, can still act as preferable pathways for gas

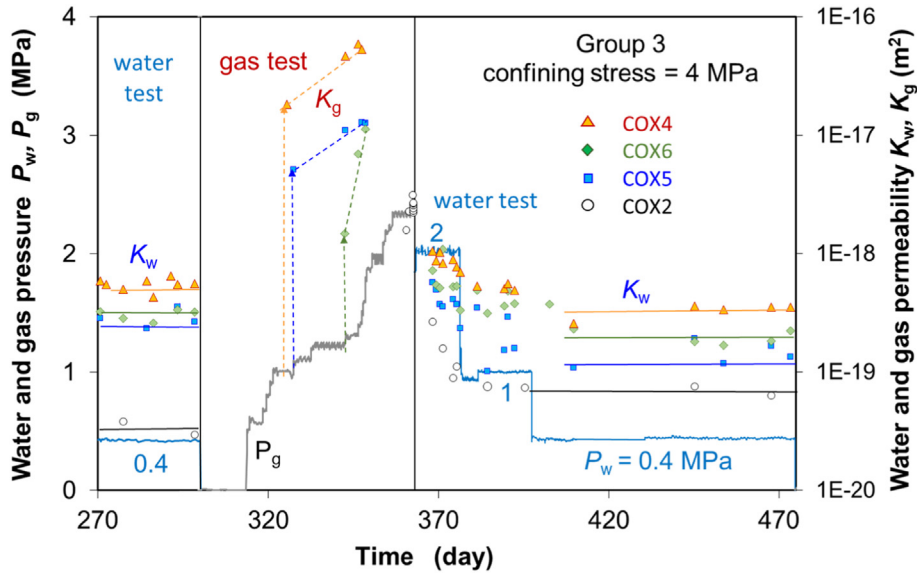


Fig. 12. Gas breakthrough pressures and permeability variations of the samples in Group 3 and resealing of gas pathways by water flow at a hydrostatic stress of 4 MPa.

Table 4
Results of measured gas breakthrough pressure P_b , water permeability before (K_{wa}) and after (K_{wb}) gas penetration through the resealed claystone samples under various confining stresses σ .

Group No.	Sample	σ (MPa)	P_b (MPa)	K_{wa} (m^2)	K_{wb} (m^2)
1	COX3	10	1.1	2×10^{-15}	—
	OPA1	10	5.5	2×10^{-19}	—
2	OPA2	13	2	3×10^{-20}	8×10^{-20}
	OPA3	13	1.3	1×10^{-18}	3×10^{-19}
3	COX2	4	2.3	3×10^{-20}	6×10^{-20}
	COX4	4	1	6×10^{-19}	3×10^{-19}
	COX5	4	1.1	3×10^{-19}	1×10^{-19}
	COX6	4	1.2	3×10^{-19}	2×10^{-19}

release without compromising the integrity and barrier functions of the host COX and OPA formations.

3.2.3. Recovery of gas-induced pathways

Recovery of gas-induced pathways was examined by measuring water permeability and comparing with that before gas penetration. The measurements were carried out at different injection pressures: $P_w = 1.4$ MPa, 1.8 MPa, and 0.9 MPa for OPA2 and OPA3 (Fig. 11); and $P_w = 2$ MPa, 1 MPa, and 0.4 MPa for COX2 and COX4-6 (Fig. 12). The injection pressures applied are significantly higher than the previous ones (0.3–0.4 MPa) before gas penetration. All samples exhibited low values of $K_w = 5 \times 10^{-19}$ – 3×10^{-20} m^2 . Most

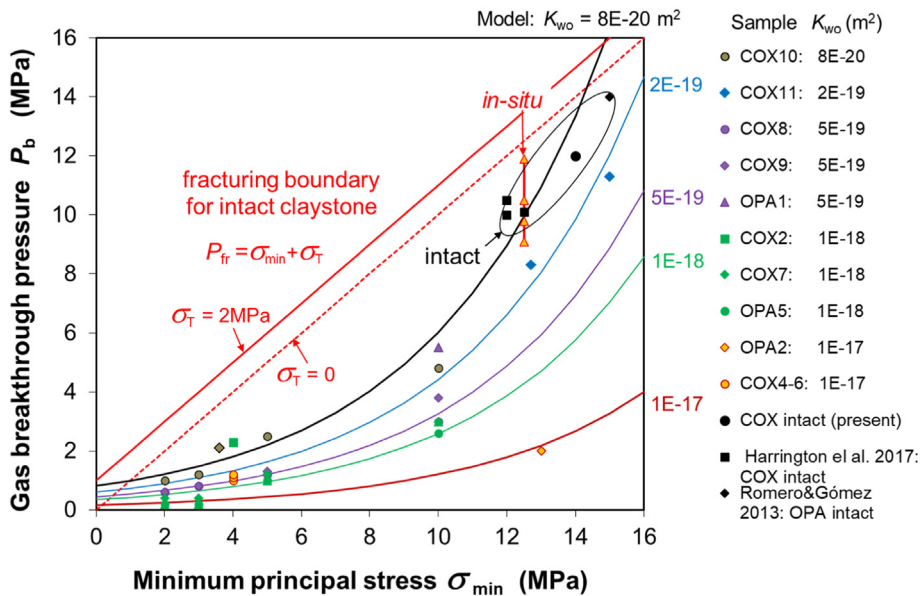


Fig. 13. Gas breakthrough pressures of the resealed and intact claystones as a function of minimum principal stress and initial water permeability.

samples (OPA3, COX4-6) showed some reduction of water permeability after gas penetration than before. This suggests that the gas-induced pathways were more consolidated with time. Only the strongly resealed samples (OPA2, COX2) showed a slight increase of K_w after gas penetration. This can be attributed to dilatancy effect induced by the applied high injection pressures. The dilatancy effect decreases with decreasing injection or pore pressure (Fig. 12). Generally, the results indicate a significant recovery of gas-induced pathways in the studied claystones.

4. Conclusions

The self-sealing capacities of different claystones (i.e. relatively rich in clay minerals, carbonates and quartz) were investigated on artificially fractured samples under various hydro-mechanical conditions by measuring fracture closure, water permeability, gas breakthrough pressure and permeability, and recovery of gas-induced pathways. The test results can lead to some important conclusions.

Under the combined impact of mechanical compression and water-induced clay swelling, the fractures in the claystones tend to seal to low water permeabilities that are close to that of the intact rock, due to their mineralogical composition, fracture intensity, confining stress, and load duration. The self-sealing capacity of the clay-rich claystone is higher than that of the carbonate-rich and sandy ones. A significant scale effect was identified, which indicates the importance of representative sample size and fracture intensity for providing reliable data for the realistic damaged rock.

The sealed fractures become gas-tight for certain pressures. The gas breakthrough pressure increases as the reciprocal of the cube root of water permeability and exponentially with increasing confining stress. However, the gas breakthrough pressures observed on the resealed and intact claystones are still lower than the applied confining stresses and cannot generate macrofractures. This implies that the EDZ is preferable route for gas release without compromising the integrity of the host rock. Furthermore, the gas-induced pathways can reseat to hinder water transport. The studied COX and OPA claystones have sufficiently high self-sealing capacities for the long-term isolation of radioactive waste.

Declaration of competing interest

The authors declare that they have no known competing financial interests or personal relationships that could have appeared to influence the work reported in this paper.

Acknowledgments

This work was co-funded by the German Federal Ministry for Economic Affairs and Energy (BMWi) under contract number 02E11627 and by the European Commission (EC) from the European Union's Horizon 2020 research and innovation program under Grant No. 847593.

References

Andra, Dossier, 2005. Synthesis–Evaluation of the feasibility of a geological repository in an argillaceous formation. <https://international.andra.fr/sites/international/files/>. (Accessed 31 March 2022).

Armand, G., Leveau, F., Nussbaum, C., de La Vaissiere, R., Noiret, A., Jaeggi, D., Landrein, P., Righini, C., 2014. Geometry and properties of the excavation-induced fractures at the Meuse/Haute-Marne URL drifts. *Rock Mech. Rock Eng.* 47 (1), 21–41.

Auvray, C., Grgic, D., Morlot, C., Fourreau, E., Talandier, J., 2015. X-ray tomography applied to self-sealing experiments on argillites. In: Proceedings of the 13th International Congress of ISRM.

Bock, H., Dehansdutter, B., Martin, C.D., Mazurek, M., de Haller, A., Skoczylas, F., Davy, C., 2010. Self-sealing of Fractures in Argillaceous Formations in the Context of Geological Disposal of Radioactive Waste—Review and Synthesis. NEA Report No. 6184. OECD.

Bossart, P., Trick, T., Meier, P.M., Mayor, J.C., 2004. Structural and hydrogeological characterisation of the excavation-disturbed zone in the Opalinus Clay (Mont Terri Project, Switzerland). *Appl. Clay Sci.* 26 (1–4), 429–448.

Bossart, P., Jaeggi, D., Nussbaum, C., 2017. Experiments on thermo-hydro-mechanical behaviour of Opalinus Clay at Mont Terri rock laboratory, Switzerland. *J. Rock Mech. Geotech. Eng.* 9 (2017), 502–510.

Conil, N., Talandier, J., Djizanne, H., de La Vaissiere, R., Righini-Waz, C., Auvray, C., Morlot, C., Armand, C., 2018. How rock samples can be representative of in-situ condition: a case study of Callovo-Oxfordian claystones. *J. Rock Mech. Geotech. Eng.* 10 (2018), 613–623.

de La Vaissiere, R., Armand, G., Talandier, J., 2015. Gas and water flow in an excavation-induced fracture network around an underground drift: a case study for a radioactive waste repository in clay rock. *J. Hydrol.* 521 (2015), 141–156.

Donna, A.D., Charrier, P., Salager, S., Bésuelle, P., 2019. Self-sealing capacity of argillite samples. In: Proceedings of the 7th International Symposium on Deformation Characteristics of Geomaterials (IS-Glasgow 2019). <https://doi.org/10.1051/e3sconf/20199203005>.

Giot, R., Auvray, A., Talandier, J., 2018. Self-sealing of claystone under X-ray nanotomography. *Geol. Soc. Spec. Publ.* 482 (1), 213–223.

Hale, S., Ries, X., Jaeggi, D., Blum, P., 2021. Mechanical and hydraulic properties of the excavation damaged zone (EDZ) in the Opalinus Clay of the Mont Terri rock laboratory, Switzerland. *Solid Earth* 12, 1581–1600.

Harrington, J.F., Cuss, R.J., Talandier, J., 2017. Gas transport properties through intact and fractured Callovo-Oxfordian mudstones. *Geol. Soc. Spec. Publ.* 454 (1), 131–154.

Horseman, S.T., Higgo, J.W., Alexander, J., Harrington, J.F., 1996. Water, Gas and Solute Movement through Argillaceous Media. Report CC-96/1. Nuclear Energy Agency.

Houben, M.E., Desbois, G., Urai, J., 2014. A comparative study of representative 2D microstructures in Shaly and Sandy facies of Opalinus Clay (Mont Terri, Switzerland) inferred from BIB-SEM and MIP methods. *Mar. Petrol. Geol.* 49 (2014), 143–161.

Kaufhold, A., Gräse, W., Plischke, I., Dohrmann, R., Siegesmund, S., 2013. Influence of carbonate content and micro fabrics on the failure strength of the sandy facies of the Opalinus Clay from Mont-Terri (Underground Rock Laboratory). *Eng. Geol.* 156, 111–118.

Marschall, P., Giger, S., de La Vaissiere, R., Shao, H., Leung, H., Nussbaum, C., Trick, T., Lanyon, B., Senger, R., Lisjak, A., Alcolea, A., 2017. Hydro-mechanical evolution of the EDZ as transport path for radionuclides and gas: insights from the Mont Terri rock laboratory (Switzerland). *Swiss J. Geosci.* 110, 173–194.

Mazurek, M., Gautschi, A., Marschall, P., Vigneron, G., Lebon, P., Delay, J., 2008. Transferability of geoscientific information from various sources (study sites, underground rock laboratories, natural analogues) to support safety cases for radioactive waste repositories in argillaceous formations. *Phys. Chem. Earth* 33, 95–105.

Nagra, 2002. Project Opalinus Clay. Safety Report. Demonstration of Disposal Feasibility for Spent Fuel, Vitrified High-Level Waste and Long-Lived Intermediate-Level Waste. Technical Report No. NTB 02-05. Nagra, Wettingen.

Pearson, F.J., Arcos, D., Bath, A., Boisson, J.Y., Fernandez, A.M., Gäbler, H.E., Gaucher, E., Grifault, L., Herman, P., Waber, H.N., 2003. Mont Terri Project—Geochemistry of water in the Opalinus Clay formation at the Mont Terri Rock Laboratory. In: Reports of the FOWG, No. 5, Bern.

Rodwell, W.R., Harris, A.W., Horseman, S.T., Lalieux, P., Müller, W., Ortiz, A.L., Pruess, K., 1999. Gas Migration and Two-phase Flow through Engineered and Geological Barriers for a Deep Repository for Radioactive Waste. A Joint EC/NEA Status Report. European Commission, EUR 19122 EN.

Robinet, J.C., Sardini, P., Siitara-Kauppi, M., Pret, D., Yven, B., 2015. Upscaling the porosity of the Callovo-Oxfordian mudstone from the pore scale to the formation scale; insights from the 3H-PMMA autoradiography technique and SEM BSE imaging. *Sediment. Geol.* 321, 1–10.

Romero, E., Gómez, R., 2013. Water and Air Permeability Tests on Deep Core Samples from Schlattingen SLA-1 Borehole. Nagra Arb. Ber. NAB 13-51. Nagra, Wettingen, Switzerland.

Thury, M., Bossart, P., 1999. Mont Terri Rock Laboratory, Results of the hydrogeological, geochemical and geotechnical experiments performed in 1996 and 1997. *Landeshydrologie und -geologie, Geologischer Bericht* No. 23. Federal Office of Topography (swisstopo), Wabern, Switzerland.

Volckaert, G., Ortiz, L., de Canniere, P., Put, M., Horseman, S.T., Harrington, J.F., Fioravante, V., Impey, M.D., 1995. MEGAS—Modelling and Experiments on Gas Migration in Repository Rocks, Final Report Phase 1, European Commission Report EUR 16235 EN.

Zhang 2010, C.L., Wiczorek, K., Xie, M.L., 2010. Swelling experiments on mudstones. *J. Rock Mech. Geotech. Eng.* 2 (1), 41–47.

Zhang, C.L., 2011. Experimental evidence for self-sealing of fractures in claystone. *Phys. Chem. Earth* 36, 1972–1980.

Zhang, C.L., 2013. Sealing of fractures in Claystone. *J. Rock Mech. Geotech. Eng.* 5, 214–220.

Zhang, C.L., 2015. Investigation of gas migration in damaged and resealed claystone. In: Shaw, R.P. (Ed.), *Gas Generation and Migration in Deep Geological Radioactive Waste Repositories*, pp. 75–93.

- Zhang, C.L., 2017. Response of clay rock to moisture change. In: Ferrari, A., Laloui, L. (Eds.), *Advances in Laboratory Testing and Modelling of Soils and Shales (ATMSS)*. Springer Nature, New York City, NY, USA.
- Zhang, C.L., Komischke, M., Kröhn, M., Rogalski, A., Zehle, B., 2019. Experimental Study of the Mechanical Behaviour of the Sandy Facies of Opalinus Clay at Mont Terri, LT-A Program within the Mont-Terri-Project. *Gesellschaft für Anlagen- und Reaktorsicherheit (GRS)*, Braunschweig, GRS-555.

und Reaktorsicherheit (GRS) - Germany's leading expert organization in the nuclear safety field. His major research interest lies in the experimental and theoretical investigations on the thermo-hydro-mechanical behaviours of different host rocks (clay, salt and granite) and clay-based barrier materials for deep geological disposal of nuclear waste.



Dr. Chun-Liang Zhang is a researcher at the Repository Safety Research Division of the Gesellschaft fuer Anlagen-